

Analytical Model of Electromagnetic Performance for Permanent-Magnet Vernier Machines Using Nonlinear Exact Conformal Model

Zhaokai Li^{ID}, Xiaoyan Huang^{ID}, *Member, IEEE*, Ang Liu^{ID}, Zixuan Liu, Lijian Wu^{ID}, *Senior Member, IEEE*, and Tingna Shi^{ID}, *Member, IEEE*

Abstract—This article investigates the air-gap field distribution of the permanent-magnet Vernier machine (PMVM) using a nonlinear exact conformal model (NECM) to account for slotting effect, flux modulation effect, and iron nonlinearity. The exact conformal model (ECM) based on the region of one-slot and one-flux-modulation-pole (OSECM) are introduced to show the effectiveness of the linear analytical model for PMVM. It can keep high calculation accuracy and significantly reduce the computational burden. Then, the NECM is developed from OSECM by introducing the equivalent saturation current into the air region and coil region. The lumped parameter magnetic circuit model (LPMCM) model is used to obtain the magnetic potential of the iron region and therefore calculate the equivalent saturation current. The NECM which combines LPMCM and OSECM can essentially improve the accuracy of the linear analytical model. The harmonic analysis of the air-gap field is performed to theoretically explain the component of electromagnetic torque. Both finite element model (FEM) simulation and test results are presented to validate the NECM.

Index Terms—Air-gap permeance, conformal transformation, iron nonlinearity, permanent-magnet vernier machines (PMVMs).

I. INTRODUCTION

THE permanent-magnet Vernier machine (PMVM) shows a significant advantage of high torque at low speed due to the magnetic gearing effect [1], [2]. Such merits make it a promising candidate for ship propulsion and electric vehicle. To efficiently optimize the performance of PMVM, significant work has been carried out on the design principle to produce steady torque [3], [4].

Generally, the flux modulation pole (FMP) is used between stator winding and permanent magnet (PM) to obtain the harmonic magnetic field with the same pole-pair numbers [5]. Although the commercial finite-element (FE) software can accurately analyze the electromagnetic performance of PMVM, there is strong demand to have a more efficient

tool for the design of PMVM at the initial stage or during optimization [6]–[8]. The high accuracy of the analytical model for permanent-magnet synchronous motors and brushless dc motors has been proven in the past decades. However, the flux leakage is much more severe due to the flux modulation, which decreases the accuracy of analytical models for PMVM.

The air-gap field modulation theory is widely used to choose the possible slot and pole combination for PMVM and give the qualitative analysis of torque component [9]–[13]. However, this method is difficult to accurately predict the air-gap field of PMVM due to neglecting its significant leakage flux. In [14], the tooth-tip flux leakage was calculated using lumped parameter magnetic circuit model (LPMCM), but its accuracy significantly depended on the prior knowledge of the leakage flux.

The subdomain model can accurately calculate the electromagnetic performance of the PM machines [15], [16]. Oner *et al.* [1] and [17] proposed an accurate subdomain model accounting for the tooth-tip region under either open-circuit or on-load conditions. In [18], the rotor eccentricity of PMVM can be analyzed by the perturbation method combined with the subdomain model and therefore the air-gap field flux density can be calculated.

The conformal transformation technique is powerful to build the relationship between the slotted and slotless air-gap field for surface-mounted PM machines [19]–[22]. There are mainly three kinds of analytical models based on conformal transformation technique: the relative permeance model (RPM) [19], the complex permeance model (CPM) [20], and the exact conformal model (ECM) [21], [22]. For PMVM, RPM was proposed in [23] and [24] to account for both slotting effect and magnetic gearing effect while CPM was used in [25] to predict both radial and tangential flux density. The accuracy of CPM is higher than RPM as the tangential component of flux density is neglected in RPM [24]. ECMs are hardly employed in the analytical analysis for PMVM in the published literature. In general, there is still no clear vision about the calculation accuracy and efficiency of conformal transformation technique for PMVM, which is important and necessary to give the researchers practical guidelines for calculating the electromagnetic performance of PMVM.

Unlike the conventional surface-mounted PM machines, PMVMs have significant leakage flux. Most analytical models

Manuscript received August 6, 2021; revised September 27, 2021; accepted October 22, 2021. Date of publication October 29, 2021; date of current version April 20, 2022. This work was supported in part by the National Natural Science Foundation of China under Grant 51922095 and in part by the National Key Research and Development Program of China under Grant 2019YFE0123500. (Corresponding author: Xiaoyan Huang.)

The authors are with the Zhejiang Provincial Key Laboratory of Electrical Machine Systems, College of Electrical Engineering, Zhejiang University, Hangzhou 310027, China (e-mail: lzk_zju@zju.edu.cn; xiaoyanhuang@zju.edu.cn; a_liu@zju.edu.cn; eelzx@zju.edu.cn; ljw@zju.edu.cn; tnsi@zju.edu.cn).

Digital Object Identifier 10.1109/TTE.2021.3124369

integrate the radial flux density along the central circle of the air-gap to predict the flux linkage [17], [24]. For some analytical models using the magnetic vector potential, it can be directly used to obtain the coil flux linkage [15]. However, there is a lack of accuracy comparison between these two methods for the flux linkage of PMVM.

The analytical models always make the assumption of infinitely permeable iron for predicting the air-gap field of PMVM, as seen in [17] and [18] and [23]–[25]. Such simplification will introduce large errors when the iron of PMVM is saturated under heavy load conditions. The nonlinear subdomain model was first proposed for surface-mounted PM machines [26], [27] and then it is applied for PMVM [28]. However, the subdomain model can only calculate the slot/tooth with an equal width angle [16]. It is difficult to derive the analytical solution of the subdomain model with irregular slot shape and non-uniform air-gap.

The hybrid field model combining CPM and LPMCM to consider the saturation effect is proposed for surface-mounted PM machines [29], [30]. However, it has low accuracy for PMVM as the CPM cannot accurately obtain the air-gap field, and the simple LPMCM shows large errors for predicting the leakage flux. The predicted leakage flux using LPMCM can be more accurate if the number of slot reluctance is increased. However, it can significantly increase the calculation time.

This article proposes the nonlinear exact conformal model (NECM) for predicting the electromagnetic performance of PMVM with higher accuracy and moderate computation time while considering iron saturation, flux leakage, slotting effect, and flux modulation effect. In the linear permeance region, one-slot and one-FMP ECM (OSECM) is the best choice to build the relationship between the air flux and current sheet distribution in terms of accuracy and efficiency. The LPMCM is used to calculate the magnetic field distribution of the iron region in the PMVM. The magnetic potential drop of stator and rotor represents the level of iron nonlinearity, which will be equivalently transformed to the saturation current sheet along the boundary between the air region and iron region. Hence, NECM is built based on the magnetic connection between OSECM and LPMCM. It shows high accuracy to predict the electromagnetic performance of PMVM due to considering flux modulation effect, slotting effect, and nonlinearity effect, which is validated by both FEM simulation and test results.

The article is organized as follows. Section II introduces the linear analytical model OSECM. Then the iron nonlinearity is represented by the equivalent saturation current and therefore NECM is derived from the OSECM in Section III. The comparisons of electromagnetic performance of PMVM using OSECM, NECM, and FEM are given in Section IV and their effectiveness is validated by the test results. The conclusion is presented in Section V.

II. ONE-SLOT AND ONE-FMP EXACT CONFORMAL MODEL

The linear analytical model using OSECM is investigated to predict the air-gap field of PMVM considering both slotting

effect and flux modulation effect. The assumptions are made as follows for the linear analytical models:

- 1) the stator and rotor iron are infinite permeable;
- 2) the property of PM is linear; and
- 3) the end effect is neglected. The iron nonlinearity is neglected in the linear analytical model and it will be considered in the NECM in Section III.

The linear analytical model using OSECM is applicable for the magnetic field produced by the dot current and therefore the PMs are equivalently transformed to the PM current in the air-gap region. For radial magnetization of PMVM, the PM current can be calculated by

$$i_{PM} = \frac{H_{c_PM} h_m}{N_{PM}} = \frac{B_r h_m}{\mu_r N_{PM}} \quad (1)$$

where h_m , H_{c_PM} , μ_r , and B_r are the thickness, coercivity, permeability, and remanence of the PM. N_{PM} is the number of PM equivalent line current on one side of the magnet. The slot current is obtained from the multiplication of phase current and the number of turns for one phase in one slot.

Then, the conformal transformation technique is used to calculate the PM current and the slot current in different domains, where the vector potentials stay unchanged. The magnetic vector potential A_{zk} at the point (r_ψ, α_ψ) in the Ψ plane which is produced by the dot current i_c at the point $(r_{c\psi}, \alpha_{c\psi})$ can be calculated according to Hague's equation

$$\begin{aligned} & A_{zk}(r_\psi, \alpha_\psi) \\ &= \frac{\mu_0 i_c}{2\pi} \left[\ln \sqrt{r_\psi^2 - 2r_\psi r_{c\psi} \cos(\alpha_\psi - \alpha_{c\psi}) + r_{c\psi}^2} \right. \\ & \quad \left. - \sum_{k=1}^{+\infty} \frac{1}{k} \left(\frac{r_{c\psi}^{2k} + r_r^{2k}}{r_s^{2k} - r_r^{2k}} \frac{r_\psi^k}{r_{c\psi}^k} + \frac{r_{c\psi}^{2k} + r_s^{2k}}{r_s^{2k} - r_r^{2k}} \frac{r_r^k}{r_\psi^k r_{c\psi}^k} \right) \right. \\ & \quad \left. \times \cos(k(\alpha_\psi - \alpha_{c\psi})) \right] \quad (2) \end{aligned}$$

where r_r and r_s are the inner and outer radius of the annular region in the Ψ plane [32]. Besides, i_c represents PM current, slot current, or equivalent saturation current that will be introduced in the next subsection. Hence, the radial and tangential flux density is given as

$$\begin{aligned} B_{\psi rc}(r_\psi, \alpha_\psi) &= \frac{\partial A_{zk}(r_\psi, \alpha_\psi)}{r_\psi \partial \alpha_\psi} \\ &= \frac{\mu_0 i_c}{2\pi} \sum_{k=1}^{\infty} h_r(r_\psi, r_{c\psi}) \sin[k(\alpha_\psi - \alpha_{c\psi})] \quad (3) \end{aligned}$$

$$\begin{aligned} B_{\psi ac}(r_\psi, \alpha_\psi) &= -\frac{\partial A_{zk}(r_\psi, \alpha_\psi)}{\partial r_\psi} \\ &= \frac{\mu_0 i_c}{2\pi} \sum_{k=0}^{\infty} h_a(r_\psi, r_{c\psi}) \cos[k(\alpha_\psi - \alpha_{c\psi})] \quad (4) \end{aligned}$$

where $h_r(r_\psi, r_{c\psi})$ and $h_a(r_\psi, r_{c\psi})$ are calculated from (2) to (4) in the Appendix.

As $B_{\psi k}$ is obtained in the Ψ plane, the logarithmic function can be used to conformally transform the annulus of the Ψ plane into the rectangle of the W plane, as shown in Fig. 1(a) and (b). The slot current and the equivalent saturation current of stator iron are uniformly distributed in the slot

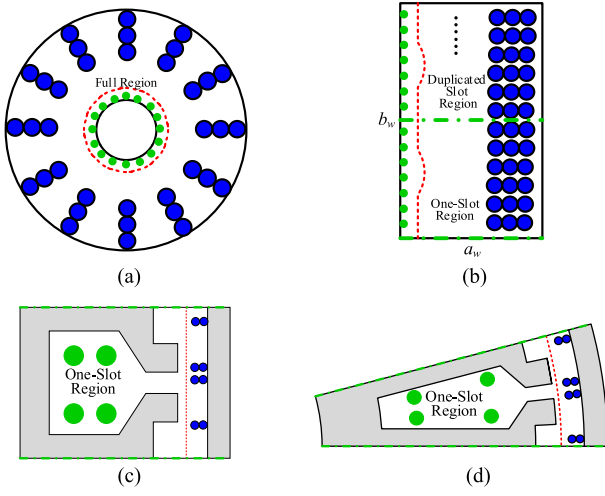


Fig. 1. One-slot and one-FMP conformal transformation process. (a) ψ plane. (b) W plane. (c) Z plane. (d) T plane.

region while the PM current and the equivalent saturation current of rotor iron are placed along the PM edge and the rotor surface, respectively. Considering the periodical air region of PMVM, only one-slot and one-FMP model is required to represent the full model based on their relative position in their corresponding slot region. The time-consuming Schwarz-Christoffel transformation can be accordingly simplified, as shown in Fig. 1(b) and (c). Finally, the exponential function is used to transform the Z plane to T plane, as shown in Fig. 1(c) and (d). Therefore, the relationship between the slotless and slotted air-gap fields is established.

Assuming the position in T plane is expressed as (r, α) and it is represented using (r_ψ, α_ψ) in the ψ plane, their relationship can be expressed as

$$\begin{aligned} r_\psi &= e^{-\frac{\pi b_w}{2} + \frac{2\pi}{a_w} \text{Im}(f^{-1}(\ln r + j\alpha))} \\ \alpha_\psi &= \pi - \frac{2\pi}{a_w} \text{Re}(f^{-1}(\ln r + j\alpha)) \end{aligned} \quad (5)$$

where a_w and b_w are the width and height of the rectangle in Fig. 1(b). They are obtained from Schwarz-Christoffel transformation through SC Toolbox in the MATLAB platform. The Schwarz-Christoffel transformation is expressed as

$$Z = f(W) = Z_0 + Z_1 \int_{w_0}^w \prod_{k=1}^{n-1} (W - w_k)^{\alpha_j - 1} dW \quad (6)$$

where Z_0 , Z_1 , α_j , and w_k are the Schwarz-Christoffel parameters from Schwarz-Christoffel transformation through SC Toolbox.

Both the position for predicting its magnetic field and the currents representing PM and the slot current in the T plane can be transformed to the corresponding position in the ψ plane. The radial and tangential flux density B_{srk} and B_{sak} in the PMVM can be conformally calculated from $B_{\psi rc}$ and $B_{\psi ac}$ based on the air-gap permeance

$$\begin{aligned} B_{srk} &= B_{\psi rc} \text{Re}(\lambda_{oe}) + B_{\psi ac} \text{Im}(\lambda_{oe}) \\ &= \frac{\mu_0 i_c}{2\pi} \left\{ \sum_{n=1}^{\infty} h_r(r_\psi, r_{c\psi}) \sin(n(\alpha_\psi - \alpha_{c\psi})) \right. \end{aligned}$$

$$\begin{aligned} &\times \sum_{k=0}^{\infty} \lambda_{oerk} \cos(k Q_s \alpha) + \sum_{n=1}^{\infty} h_a(r_\psi, r_{c\psi}) \\ &\cdot \cos(n(\alpha_\psi - \alpha_{c\psi})) \sum_{k=1}^{\infty} \lambda_{oeik} \sin(k Q_s \alpha) \left. \right\} \quad (7) \end{aligned}$$

$$\begin{aligned} B_{sak} &= B_{\psi ac} \text{Re}(\lambda_{oe}) - B_{\psi rc} \text{Im}(\lambda_{oe}) \\ &= \frac{\mu_0 i_c}{2\pi} \left\{ \sum_{n=1}^{\infty} h_a(r_\psi, r_{c\psi}) \cos(n(\alpha_\psi - \alpha_{c\psi})) \right. \\ &\times \sum_{k=0}^{\infty} \lambda_{oerk} \cos(k Q_s \alpha) - \sum_{n=1}^{\infty} h_r(r_\psi, r_{c\psi}) \\ &\times \sin(n(\alpha_\psi - \alpha_{c\psi})) \sum_{k=1}^{\infty} \lambda_{oeik} \sin(k Q_s \alpha) \left. \right\} \quad (8) \end{aligned}$$

where λ_{oerk} and λ_{oeik} are the Fourier of the real part and imaginary part of the air-gap permeance λ_{oe} . Q_s is the slot number

$$\begin{aligned} \lambda_{oe}(r, \alpha) &= \frac{j a_w}{2\pi f'(w) r_\psi} e^{j(\alpha - \alpha_\psi)} \\ &= \sum_{k=0}^{\infty} \lambda_{oerk} \cos(k Q_s \alpha) + j \sum_{k=1}^{\infty} \lambda_{oeik} \sin(k Q_s \alpha) \quad (9) \end{aligned}$$

where $f'(w)$ represents the derivative of the Schwarz-Christoffel transformation $f(w)$ to the variable w . It is calculated using the command `evadiff(f, w)` in SC Toolbox. When the position of PM current changes due to rotation of PMVM, the updated flux density B_{srk} and B_{sak} can be obtained from the linear interpolation method since many possible positions of PM current are obtained along the one-slot and one-FMP span at the beginning, as shown in Fig. 1. In consequence, it can significantly reduce the computational burden.

III. NONLINEAR EXACT CONFORMAL MODEL

ECM combined with LPMCM is used for surface-mounted PM motor. However, its leakage flux is neglected in the LPMCM since it is small [33]. Unlike the surface-mounted PM motors, there is significant leakage flux in PMVM. Hence, this article firstly proposed that the ECM is used to calculate the leakage flux of PMVM in Section II and the leakage flux source is introduced to consider its influence on stator iron saturation in LPMCM, Fig. 2. The air-gap flux source and slot flux source produced by PM and winding current are obtained from the solution of OSECM and therefore the LPMCM can be solved accordingly

$$\phi_{k_m} = l_{ef} [A_{zk_m} - A_{z(k_m+1)}] \quad (10)$$

where A_{zk_m} and $A_{z(k_m+1)}$ are the vector potential near the iron region. l_{ef} is the effective length of the PMVM.

In Fig. 2, the magnetic reluctance is established using the conception of flux tube [34]. According to Kirchhoff's law, the general solution of magnetic potential matrix Ψ for NECM is given as

$$f(\Psi) = \mathbf{A} \mathbf{A} \mathbf{A}^T \Psi - \Phi_{\text{iron}} = \mathbf{0} \quad (11)$$

where \mathbf{A} is the incidence matrix obtained from the LPMCM and \mathbf{A} represents the iron reluctance matrix. Φ_{iron} is the flux

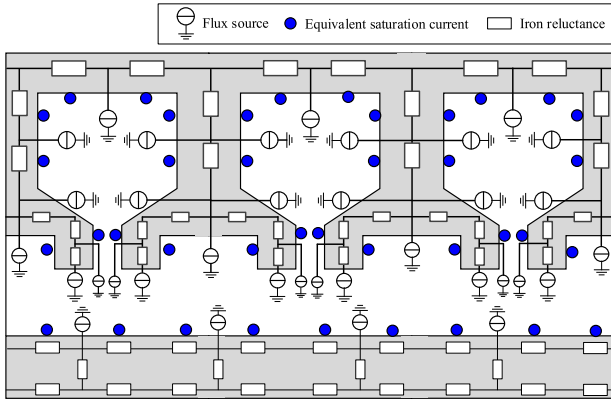


Fig. 2. Overview of NECM for predicting the saturated field distribution.

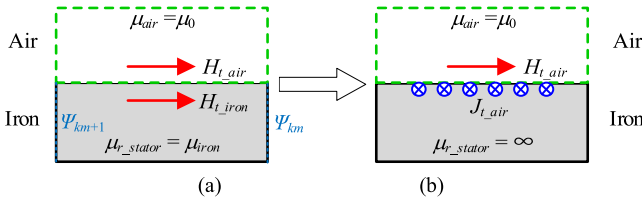


Fig. 3. Equivalence of air field distribution between (a) nonlinearly permeable iron and (b) infinitely permeable iron.

source matrix produced by the equivalent current including PM, stator winding, and iron saturation.

There is an equivalence between the saturation current and the magnetic potential drop on the boundary of the air-gap region and coil region, Fig. 3. According to the magnetic boundary condition, the tangential magnetic field strength is continuous across the interface between air and iron, where $H_{t,air} = H_{t,iron}$ is obtained in Fig. 3(a). Then, if the iron permeability is assumed infinite, the virtual current sheet representing iron nonlinearity is introduced to satisfy the magnetic boundary condition and keep the air field unchanged. The value of tangential magnetic field strength should be equal to that of the virtual current sheet. Hence, the equivalent saturation current can be obtained from the magnetic potential drop

$$i_{ck_m} = \Psi_{k_m} - \Psi_{k_m+1} \quad (12)$$

where Ψ_{k_m} and Ψ_{k_m+1} are the magnetic potentials in the iron region of Fig. 3 along the tangential direction.

It is noted that the iron region in Fig. 3 can be used to represent the iron of stator yoke, stator tooth, FMP, and rotor surface. Hence, the equivalent saturation current for PMVM can be found using the blue dot in Fig. 2, whose value is equal to the magnetic potential drop of the corresponding magnetic reluctance. According to (2), (10)–(12), the general expression of NECM for PMVM is manipulated as

$$f(\Psi) = (\mathbf{A}\mathbf{A}^T - \mathbf{PE}_0)\Psi - \Phi_{PM} - \Phi_{winding} = \mathbf{0} \quad (13)$$

where Φ_{PM} and $\Phi_{winding}$ are the flux source matrix produced by PM and winding neglecting iron nonlinearity. They can be obtained from (2). \mathbf{E}_0 is the constant matrix from (10)

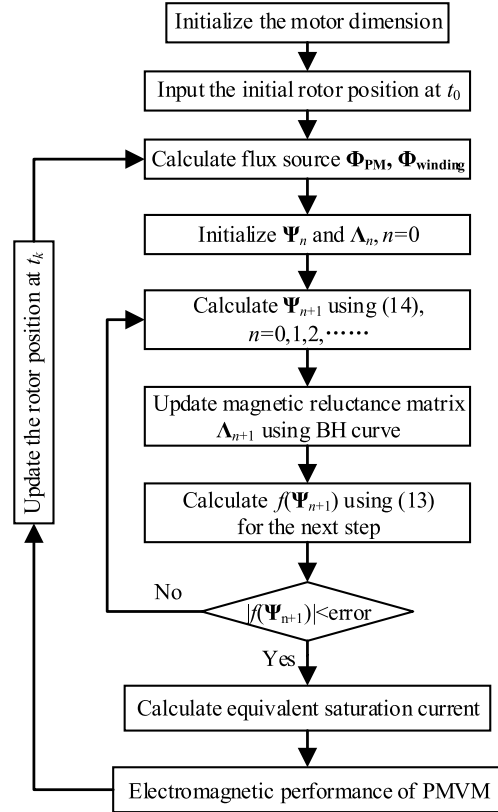


Fig. 4. Calculation flowchart of NECM for PMVM.

to (12). \mathbf{P} is the magnetic vector potential matrix from (2) which represents the relationship between the flux value and dot current position.

In order to obtain the nonlinear value of \mathbf{A} in (13), a solving loop is established to calculate the magnetic field of PMVM using the Newton-Raphson method, Fig. 4. The Newton-Raphson's iteration between Ψ_{n+1} and Ψ_n is manipulated as

$$\Psi_{n+1} = \Psi_n - \alpha_r (\mathbf{A}\mathbf{A}^T - \mathbf{PE}_0)^{-1} f(\Psi_n) \quad (14)$$

where α_r is the relaxation factor to accelerate the convergence of the iterative calculation.

IV. FINITE-ELEMENT AND EXPERIMENTAL COMPARISON

The 56-pole/18-slot PMVM with two FMPs per tooth is designed to compare accuracy between linear and nonlinear analytical models. The overhang structure is used to increase the output torque, as shown in Fig. 5. Therefore, the iron nonlinearity becomes severe in the stator yoke and tooth region due to the reduction of axial length. The open-circuit flux density distribution of PMVM is shown in Fig. 6. The main parameters of the prototype are shown in Table I. The PM is fan-shaped with radial magnetization. The electrical steel for stator yoke, stator tooth, and rotor yoke is 50WW350 while the FMP uses soft magnetic material Somaloy700. Their BH curve is shown in Fig. 7. The performance of the prototype PMVM is measured in the test rig to validate the proposed models, as shown in Fig. 8.

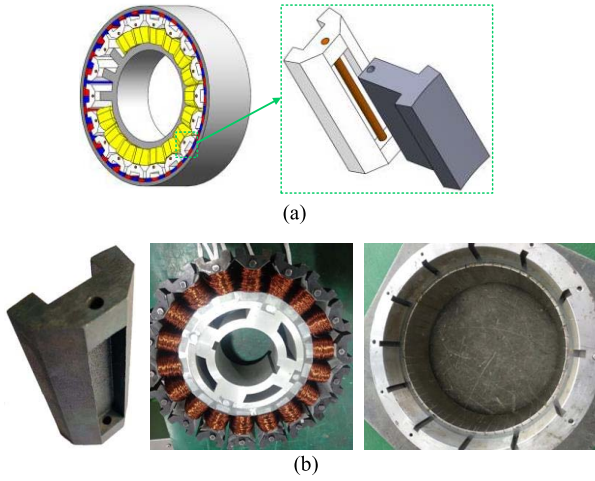


Fig. 5. Geometric structure of PMVM with tooth-shoe overhang. (a) CAD model. (b) Prototype.

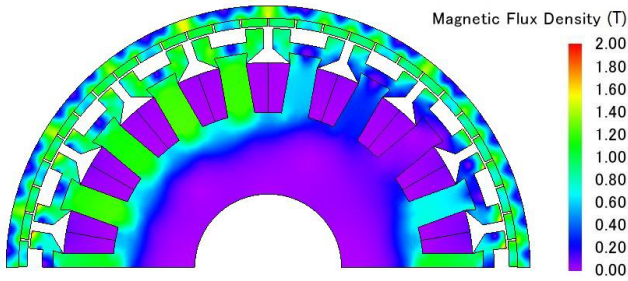


Fig. 6. On-load flux density distribution of PMVM using commercial FE software JMAG.

TABLE I
MAIN PARAMETERS OF PMVM

Parameter	Value	Parameter	Value
Pole number	56	Slot number	18
Stator outer radius	114mm	Rotor outer radius	125mm
Stator inner radius	35mm	Rotor inner radius	119mm
Stator yoke height	39mm	PM thickness	4mm
Tooth width	13mm	Pole arc coefficient	0.93
Tooth height	34.12mm	Magnet remanence	1.23T
Slot opening	4.69mm	Width of FMP	7mm
Axial length of rotor, PM, tooth-shoe and FMP	80mm	Axial length of stator yoke and stator tooth	60mm
Rated speed	600rpm	Rated current (rms)	20A

A. Air-Gap Field

In order to validate the accuracy and efficiency of OSECM, the whole ECM and single-slot/FMP ECM are introduced to show the interaction between slot and FMP. According to (7), the accuracy of the air-gap field for PMVM using ECM is mainly affected by the air-gap permeance and dot current position in the Ψ plane. Hence, the comparison of ECMs for predicting the air-gap permeance and dot current position is shown in Figs. 9 and 10. The whole ECM conformally transforms the whole air region and coil region, which is the most

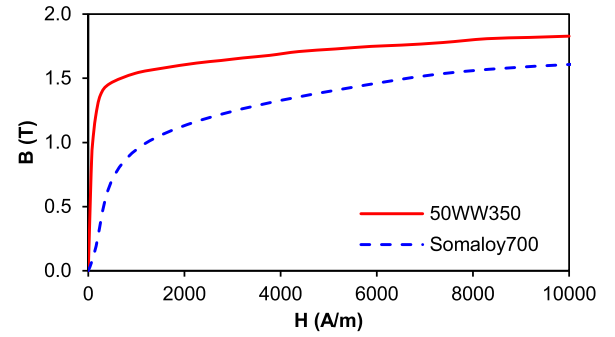


Fig. 7. BH curves of magnetic material for PMVM.

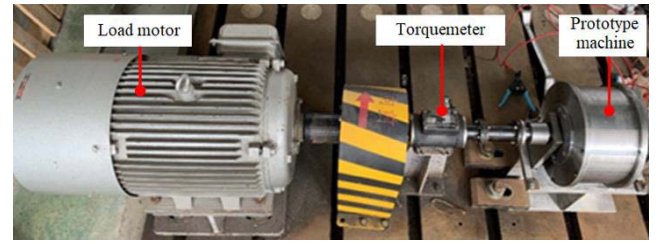


Fig. 8. Experimental setup for prototype PMVM.

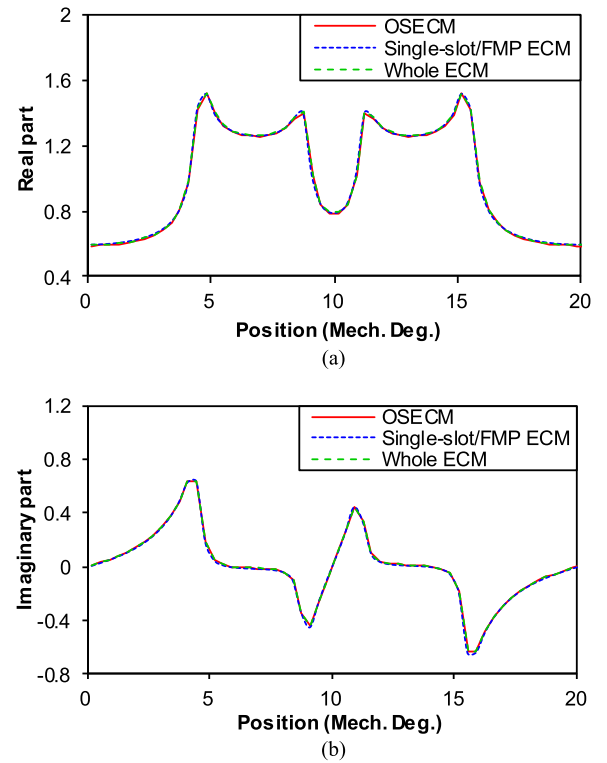


Fig. 9. Comparison of complex air-gap permeance. (a) Real part. (b) Imaginary part.

accurate among these ECMs. As for single-slot/FMP ECM, the slot region and FMP region are mapped separately neglecting the interaction between slot and FMP. It can be seen that these ECMs agree well with each other in air-gap permeance, which means that the interaction between slot and FMP has negligible

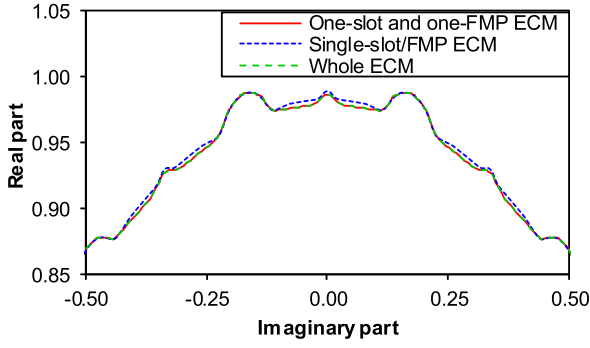


Fig. 10. Comparison of the current position in Ψ plane.

influence on the air-gap permeance. However, single-slot/FMP ECM shows large errors in calculating the current position in Ψ plane, leading to large errors for predicting the air-gap field. The calculation time for the OSECM, the whole ECM, and single-slot/FMP ECM is 0.86, 11.40, and 1.35 s, respectively. As OSECM has similar accuracy to that of whole ECM and reduces much calculation, it is used in the NECM to obtain the analytical air-gap field.

For the on-load air-gap flux density, the single-slot/FMP ECM shows the largest errors while OSECM can achieve high accuracy, Figs. 11 and 12. According to the analytical model, the major harmonic component of flux density can be obtained, of which the 14th harmonic dominates. The errors of fundamental flux density in radial and tangential directions are 2.8% and 2.3% for OSECM, respectively, while they are 1.6% and 0.4% for NECM.

B. Flux Linkage and Back EMF

There are mainly two methods to calculate the flux linkage of each phase for PMVM based on analytical models. The first method (M1) is to integrate the radial air-gap flux density along the stator bore [24]

$$\varphi_{ph}(t) = N_c \sum_{coil} R_{s l_{ef}} \int_{\alpha_i - \tau/2}^{\alpha_i + \tau/2} B_{sr}(R_s, \alpha) d\alpha \quad (15)$$

where N_c is the number of turns for each phase. α_i is the coil center and τ is the coil span. The flux leakage of PMVM is neglected using (15) and therefore large errors are introduced using either OSECM or NECM. The other method (M2) to calculate the flux linkage is based on the magnetic vector potential of each coil

$$\varphi_{ph}(t) = N_c \sum_{coil} l_{ef} [A_{zc} - A_{z(c+1)}] \quad (16)$$

where A_{zc} and $A_{z(c+1)}$ are the magnetic vector potential of the coil belonging to the same phase.

As shown in Fig. 13, the flux linkages using M2 are more accurate than those using M1 based on either OSECM or NECM. NECM-M2 (NECM combined with M2 for calculating flux linkage) has the best accuracy due to considering both the nonlinearity effect and flux leakage. In Fig. 14, both OSECM and NECM will underestimate the flux linkage using M1 due to neglecting flux leakage. The NECM-M2

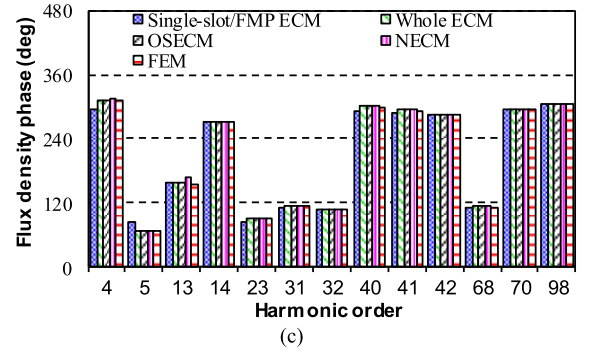
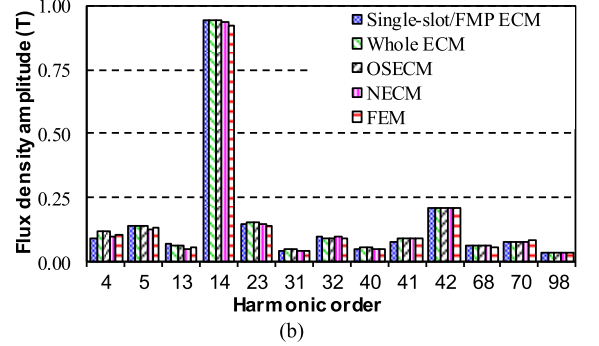
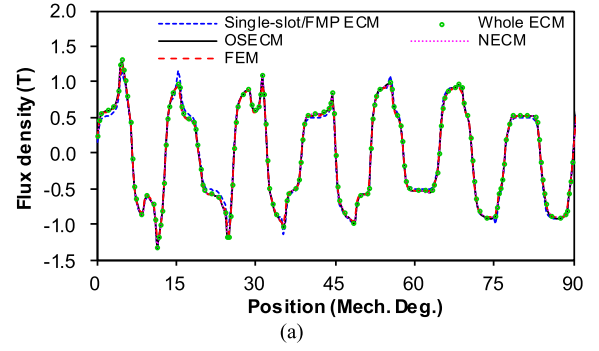


Fig. 11. Radial air-gap flux density distribution at rated load. (a) Flux density waveform. (b) Major harmonic amplitude. (c) Major harmonic phase.

calculations still agree well with FEM results at different input currents. Hence, M2 is more suitable to predict the flux linkage in the analytical models for PMVM.

The back EMF is obtained from the derivative of flux linkage to time

$$E_{ph} = -\frac{d\varphi_{ph}}{dt} \quad (17)$$

Thus, the accuracy of back EMF depends on the calculation of flux linkage. As shown in Fig. 15, the predicted back EMF using OSECM are larger than measured back EMF due to the assumption of infinitely permeable iron while NECM prediction agrees well with measured back EMF.

C. Electromagnetic Torque

For the analytical model based on conformal transformation, the electromagnetic torque is calculated using Maxwell tensor theory [20]

$$T_{ce} = \frac{1}{\mu_0} l_{ef} r^2 \int_0^{2\pi} B_{sr}(\alpha, r) B_{sa}(\alpha, r) d\alpha$$

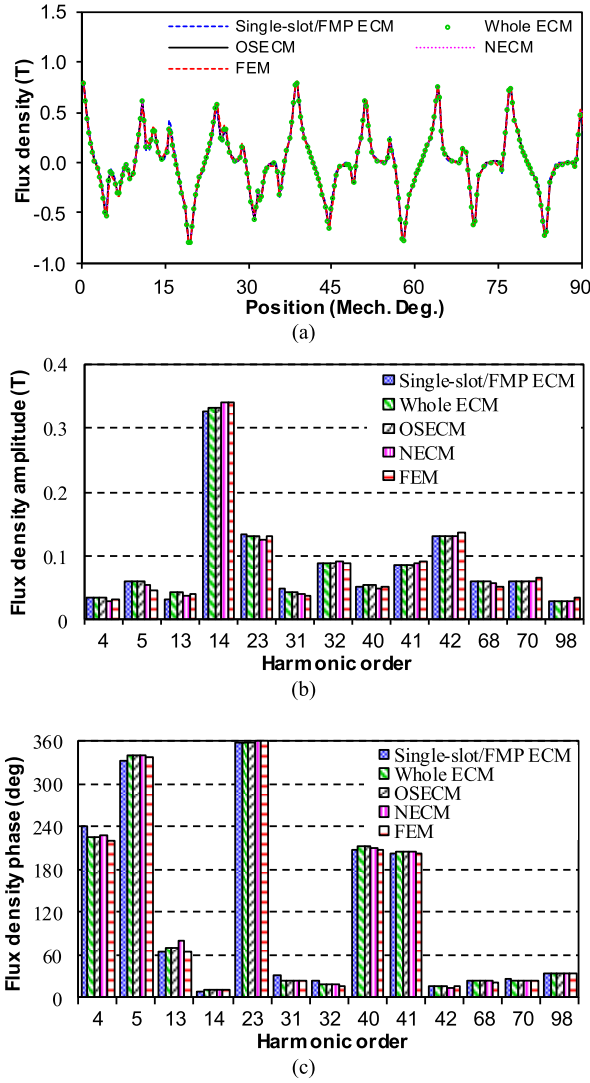


Fig. 12. Tangential air-gap flux density distribution at rated load. (a) Flux density waveform. (b) Major harmonic amplitude. (c) Major harmonic phase.

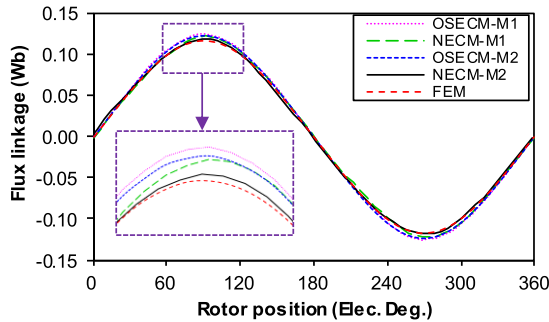


Fig. 13. Flux linkage waveform of PMVM under open-circuit condition.

$$= \frac{1}{2\mu_0} l_{ef} r^2 \sum_{n=1}^{\infty} B_m B_{an} \cos(\alpha_{an} - \alpha_m) \quad (18)$$

where B_{sr} and B_{sa} can be replaced by the flux density obtained in (7) and (8) for either OSECM or NECM. B_m , B_{an} , α_m , and

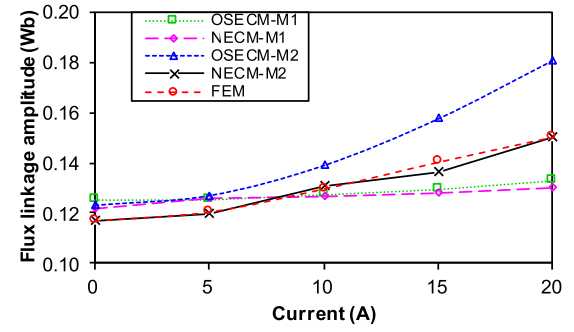


Fig. 14. Variation of flux linkage amplitude with the winding current for PMVM.

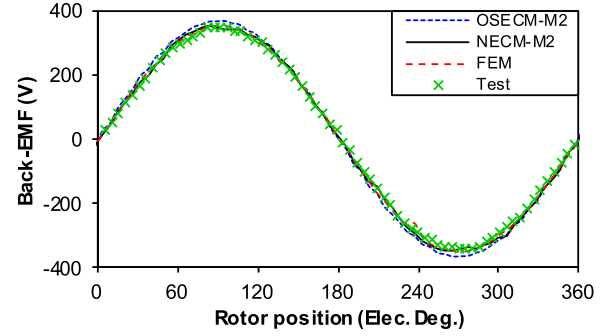


Fig. 15. Back EMF waveform of PMVM under open-circuit condition.

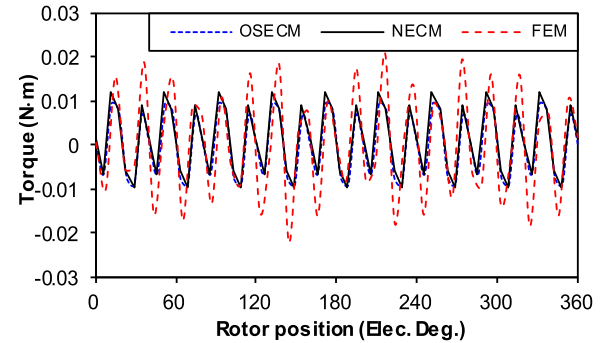


Fig. 16. Cogging torque waveform of PMVM.

α_{an} are the harmonic amplitude and phase of B_{sr} and B_{sa} from (7) to (8).

As the iron of PMVM is not saturated at open-circuit conditions, the iron nonlinearity has negligible influence on the cogging torque, as shown in Fig. 16. Hence, both OSECM and NECM can accurately predict the cogging torque. As for the rated torque, the iron of PMVM reaches the saturation level due to the armature reaction field. Therefore, it will decrease the rated torque. Accordingly, as shown in Fig. 17, OSECM overestimates the torque value but NECM still achieves high accuracy. Besides, the comparison of torque harmonic is investigated in Table II. It can be seen that the 14th harmonic flux density plays a major role in producing the electromagnetic torque, which is the result of flux modulation. The other harmonic, such as the 13th harmonic flux density, only produces less than 0.2% of the total torque in Table II.

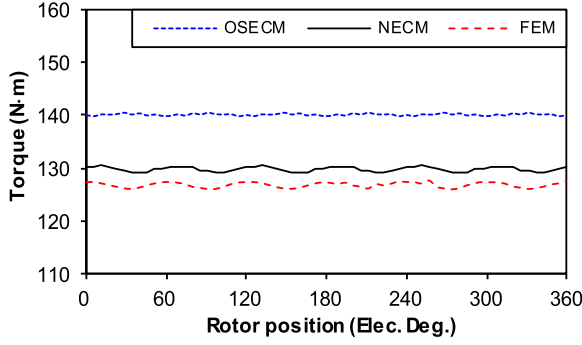


Fig. 17. Torque waveform of PMVM at rated load.

TABLE II
HARMONIC COMPONENT OF TORQUE USING THE HARMONIC FLUX
DENSITY FOR PMVM (UNIT: N · M)

Harmonic order	OSECM	NECM	FEM
4	-0.40	-0.36	0.02
5	-1.31	-1.19	0.01
13	-0.16	-0.15	-0.01
14	141.56	131.64	126.84
23	0.56	0.51	0.03
31	0.00	0.00	0.00
32	-0.08	-0.07	0.04
40	0.01	0.01	0.00
41	0.01	0.00	0.02
Total	140.17	130.16	126.97

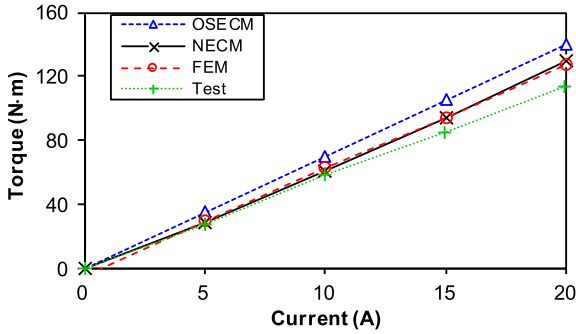


Fig. 18. Variation of average torque with winding current for PMVM.

Therefore, the errors of other harmonic flux densities have a negligible influence on the electromagnetic torque. Fig. 18 shows the average electromagnetic torque of PMVM with different current amplitudes. OSECM overestimates the average torque at different current amplitude and the errors are larger than 19%. NECM agrees well with FEM and test results at small current amplitude, whose errors are less than 5% when the input current $I_m \leq 10$ A. However, larger errors occur for both NECM and FEM at large current amplitude due to neglecting the end effect of PMVM, which will be investigated and improved in future work.

D. Calculation Time

The OSECM can significantly reduce the computational burden due to neglecting iron saturation, as shown in Table III,

TABLE III
CALCULATION TIME OF ANALYTICAL MODELS AND
FEM FOR PMVM (UNIT: s)

Current (A)	OSECM	NECM	FEM
0	13.0	181	1962
5	12.8	180	2098
10	12.9	203	2562
15	12.9	198	2526
20	12.9	214	2540

since there is no iterative process of solving the nonlinear iron permeability in OSECM. The main configuration of the computer is Intel i9-9900 CPU@3.10 GHz with 32 GB memory. The tangential division for OSECM, NECM, and FEM is 360 and the time step is 50. The mesh node of FEM is 13 170. The NECM predictions are close to the FEM results, but it only requires less than 1/10 calculation time of FEM, which is given in Table III. Hence, the NECM can be a competitive candidate for the analysis of PMVM in terms of calculation accuracy and efficiency. Both OSECM and NECM show a proper tradeoff between accuracy and efficiency.

V. CONCLUSION

In this article, the analytical model based on nonlinear conformal transformation is investigated for PMVM to achieve high calculation accuracy and high efficiency. In terms of the tradeoff between accuracy and efficiency, the OSECM is proposed to predict the performance of PMVM accounting for large flux leakage. It builds up the relationship between the air-gap field and the equivalent current of PM, winding, and iron nonlinearity. In order to obtain the equivalent current of iron nonlinearity in the analytical model, the LPMCM is used to show the saturation level of the stator and rotor. Thus, the equivalent current of iron nonlinearity which is extracted from the magnetic potential distribution of LPMCM is utilized to account for the saturation effect. The high accuracy and high efficiency of NECM are verified by both FEM and test results, which makes the proposed model a powerful tool for designing PMVM for the application of ship propulsion and electric vehicle.

APPENDIX

The calculation of $h_r(r_\psi, r_{c\psi})$ and $h_a(r_\psi, r_{c\psi})$ are given as

$$h_r(r_\psi, r_{c\psi}) = \begin{cases} \frac{r_{c\psi}}{r_\psi^2 - 2r_\psi r_{c\psi} \cos(\alpha_\psi - \alpha_{c\psi}) + r_{c\psi}^2} \\ + \left(\frac{r_{c\psi}^2 + r_r^2}{r_{c\psi}(r_s^2 - r_r^2)} + \frac{r_{c\psi}^2 + r_s^2}{r_s^2 - r_r^2} \frac{r_r^2}{r_\psi^2 r_{c\psi}} \right), & k = 1 \\ \left(\frac{r_{c\psi}^{2k} + r_r^{2k}}{r_s^{2k} - r_r^{2k}} \frac{r_\psi^k}{r_{c\psi}^k} + \frac{r_{c\psi}^{2k} + r_s^{2k}}{r_s^{2k} - r_r^{2k}} \frac{r_r^{2k}}{r_\psi^k r_{c\psi}^k} \right), & k > 1 \end{cases} \quad (19)$$

$$h_{\alpha}(r_{\psi}, r_{c\psi}) = \begin{cases} -\frac{r_{\psi}}{r_{\psi}^2 - 2r_{\psi}r_{c\psi}\cos(\alpha_{\psi} - \alpha_{c\psi}) + r_{c\psi}^2}, & k = 0 \\ \frac{r_{c\psi}}{r_{\psi}^2 - 2r_{\psi}r_{c\psi}\cos(\alpha_{\psi} - \alpha_{c\psi}) + r_{c\psi}^2} \\ + \left(\frac{r_{c\psi}^{2k} + r_r^2}{r_{c\psi}(r_s^2 - r_r^2)} - \frac{r_{c\psi}^2 + r_s^2}{r_s^2 - r_r^2} \frac{r_r^2}{r_{\psi}^2 r_{c\psi}} \right), & k = 1 \\ \frac{r_{c\psi}^{2k} + r_r^{2k}}{r_s^{2k} - r_r^{2k}} \frac{r_{\psi}^{k-1}}{r_{c\psi}^k} - \frac{r_{c\psi}^{2k} + r_s^{2k}}{r_s^{2k} - r_r^{2k}} \frac{r_r^{k+1}}{r_{\psi}^{k+1} r_{c\psi}^k}, & k > 1. \end{cases} \quad (20)$$

REFERENCES

- [1] Y. Oner, Z. Q. Zhu, L. J. Wu, X. Ge, H. L. Zhan, and J. T. Chen, "Analytical on-load subdomain field model of permanent-magnet Vernier machines," *IEEE Trans. Ind. Electron.*, vol. 63, no. 7, pp. 4105–4117, Jul. 2016.
- [2] D. Wu, Z. Xiang, X. Zhu, L. Quan, M. Jiang, and Y. Liu, "Optimization design of power factor for an in-wheel Vernier PM machine from perspective of air-gap harmonic modulation," *IEEE Trans. Ind. Electron.*, vol. 68, no. 10, pp. 9265–9276, Oct. 2021.
- [3] X. Zhao and S. Niu, "A new slot-PM Vernier reluctance machine with enhanced zero-sequence current excitation for electric vehicle propulsion," *IEEE Trans. Ind. Electron.*, vol. 67, no. 5, pp. 3528–3539, May 2020.
- [4] L. Xu, G. Liu, W. Zhao, X. Yang, and R. Cheng, "Hybrid stator design of fault-tolerant permanent-magnet Vernier machines for direct-drive applications," *IEEE Trans. Ind. Electron.*, vol. 64, no. 1, pp. 179–190, Jan. 2017.
- [5] Y. Yu, F. Chai, Y. Pei, and L. Chen, "Comparisons of torque performance in surface-mounted PM Vernier machines with different stator tooth topologies," *IEEE Trans. Ind. Appl.*, vol. 55, no. 4, pp. 3671–3684, Jul. 2019.
- [6] S.-U. Chung, J.-W. Kim, B.-C. Woo, D.-K. Hong, J.-Y. Lee, and D.-H. Koo, "A novel design of modular three-phase permanent magnet Vernier machine with consequent pole rotor," *IEEE Trans. Magn.*, vol. 47, no. 10, pp. 4215–4218, Oct. 2011.
- [7] L. Li, W. N. Fu, S. L. Ho, S. Niu, and Y. Li, "A quantitative comparison study of power-electronic-driven flux-modulated machines using magnetic field and thermal field co-simulation," *IEEE Trans. Ind. Electron.*, vol. 62, no. 10, pp. 6076–6084, Oct. 2015.
- [8] J. Yang *et al.*, "Quantitative comparison for fractional-slot concentrated-winding configurations of permanent-magnet Vernier machines," *IEEE Trans. Magn.*, vol. 49, no. 7, pp. 3826–3829, Jul. 2013.
- [9] H. Li, Z. Q. Zhu, and Y. Liu, "Optimal number of flux modulation pole in Vernier permanent magnet synchronous machines," *IEEE Trans. Ind. Appl.*, vol. 55, no. 6, pp. 5747–5757, Nov. 2019.
- [10] P. M. Tlali, R.-J. Wang, S. Gerber, C. D. Botha, and M. J. Kamper, "Design and performance comparison of Vernier and conventional PM synchronous wind generators," *IEEE Trans. Ind. Appl.*, vol. 56, no. 3, pp. 2570–2579, May 2020.
- [11] D. Li, R. Qu, and Z. Zhu, "Comparison of Halbach and dual-side Vernier permanent magnet machines," *IEEE Trans. Magn.*, vol. 50, no. 2, pp. 801–804, Feb. 2014.
- [12] Z. Wu, Y. Fan, Q. Zhang, and D. Gao, "Comparison and analysis of permanent magnet Vernier motors for low-noise in-wheel motor application," *IET Electr. Power Appl.*, vol. 14, no. 2, pp. 274–281, Feb. 2020.
- [13] J. Bai, P. Zheng, C. Tong, Z. Song, and Q. Zhao, "Characteristic analysis and verification of the magnetic-field-modulated brushless double-rotor machine," *IEEE Trans. Ind. Electron.*, vol. 62, no. 7, pp. 4023–4033, Jul. 2015.
- [14] W. Li, K. T. Chau, C. Liu, S. Gao, and D. Wu, "Analysis of tooth-tip flux leakage in surface-mounted permanent magnet linear Vernier machines," *IEEE Trans. Magn.*, vol. 49, no. 7, pp. 3949–3952, Jul. 2013.
- [15] L. J. Wu, Z. Q. Zhu, D. Staton, M. Popescu, and D. Hawkins, "Analytical prediction of electromagnetic performance of surface-mounted PM machines based on subdomain model accounting for tooth-tips," *IET Electr. Power Appl.*, vol. 5, no. 7, p. 597, 2011.
- [16] L. J. Wu, Z. Q. Zhu, D. Staton, M. Popescu, and D. Hawkins, "An improved subdomain model for predicting magnetic field of surface-mounted permanent magnet machines accounting for tooth-tips," *IEEE Trans. Magn.*, vol. 47, no. 6, pp. 1693–1704, Jun. 2011.
- [17] Y. Oner, Z. Q. Zhu, L. J. Wu, and X. Ge, "Analytical sub-domain model for predicting open-circuit field of permanent magnet Vernier machine accounting for tooth tips," *COMPEL: Int. J. Comput. Math. Electr. Electron. Eng.*, vol. 35, no. 2, pp. 624–640, Mar. 2016.
- [18] Y. Yang, B. Yan, N. Wang, and X. Wang, "Analytical prediction of electromagnetic performance of Vernier machine with rotor eccentricity," *Electr. Power Compon. Syst.*, vol. 44, no. 15, pp. 1693–1706, 2016.
- [19] Q. Zhu and D. Howe, "Instantaneous magnetic field distribution in brushless permanent magnet DC motors. III. Effect of stator slotting," *IEEE Trans. Magn.*, vol. 29, no. 1, pp. 143–151, Jan. 1993.
- [20] D. Žarko, D. Ban, and T. A. Lipo, "Analytical solution for cogging torque in surface permanent-magnet motors using conformal mapping," *IEEE Trans. Magn.*, vol. 44, no. 1, pp. 52–65, Jan. 2008.
- [21] T. C. O'Connell and P. T. Krein, "A Schwarz–Christoffel-based analytical method for electric machine field analysis," *IEEE Trans. Energy Convers.*, vol. 24, no. 3, pp. 565–577, Sep. 2009.
- [22] K. Ramakrishnan, D. Zarko, A. Hanic, and G. Mastinu, "Improved method for field analysis of surface permanent magnet machines using Schwarz–Christoffel transformation," *IET Electr. Power Appl.*, vol. 11, no. 6, pp. 1067–1075, Jul. 2017.
- [23] S. Hyoseok, N. Niguchi, and K. Hirata, "Characteristic analysis of surface permanent-magnet Vernier motor according to pole ratio and winding pole number," *IEEE Trans. Magn.*, vol. 53, no. 11, pp. 1–4, Nov. 2017.
- [24] M. Choi and B. Kim, "Calculation of PM Vernier motors using an improved air-gap permeance function," *IEEE Trans. Magn.*, vol. 55, no. 6, pp. 1–5, Jun. 2019.
- [25] J. Li, K. T. Chau, and W. Li, "Harmonic analysis and comparison of permanent magnet Vernier and magnetic-gear machines," *IEEE Trans. Magn.*, vol. 47, no. 10, pp. 3649–3652, Oct. 2011.
- [26] L. Wu, H. Yin, D. Wang, and Y. Fang, "A nonlinear subdomain and magnetic circuit hybrid model for open-circuit field prediction in surface-mounted PM machines," *IEEE Trans. Energy Convers.*, vol. 34, no. 3, pp. 1485–1495, Sep. 2019.
- [27] L. Wu, H. Yin, D. Wang, and Y. Fang, "On-load field prediction in SPM machines by a subdomain and magnetic circuit hybrid model," *IEEE Trans. Ind. Electron.*, vol. 67, no. 9, pp. 7190–7201, Sep. 2020.
- [28] Y. Zhu, G. Liu, L. Xu, W. Zhao, and D. Cao, "A hybrid analytical model for permanent magnet Vernier machines considering saturation effect," *IEEE Trans. Ind. Electron.*, vol. 69, no. 2, pp. 1211–1223, Feb. 2022.
- [29] L. J. Wu, Z. Li, X. Huang, Y. Zhong, Y. Fang, and Z. Q. Zhu, "A hybrid field model for open-circuit field prediction in surface-mounted PM machines considering saturation," *IEEE Trans. Magn.*, vol. 54, no. 6, pp. 1–12, Jun. 2018.
- [30] L. J. Wu, Z. Li, D. Wang, H. Yin, X. Huang, and Z. Q. Zhu, "On-load field prediction of surface-mounted PM machines considering nonlinearity based on hybrid field model," *IEEE Trans. Magn.*, vol. 55, no. 3, pp. 1–11, Mar. 2019.
- [31] Z. Q. Zhu, D. Howe, and C. C. Chan, "Improved analytical model for predicting the magnetic field distribution in brushless permanent-magnet machines," *IEEE Trans. Magn.*, vol. 38, no. 1, pp. 229–238, Jan. 2002.
- [32] B. Hague, *Electromagnetic Problems in Electrical Engineering*. London, U.K.: Oxford Univ. Press, 1929.
- [33] A. Hanic, D. Žarko, D. Kuhinek, and Z. Hanic, "On-load analysis of saturated surface permanent magnet machines using conformal mapping and magnetic equivalent circuits," *IEEE Trans. Energy Convers.*, vol. 33, no. 3, pp. 915–924, Sep. 2018.
- [34] V. Ostovic, *Dynamics of Saturated Electric Machines*. New York, NY, USA: Springer, 1989.



Zhaokai Li was born in Lishui, China, in 1993. He received the B.S. and Ph.D. degrees in electrical engineering from Zhejiang University, Hangzhou, China, in 2015 and 2020, respectively.

He is currently a Post-Doctoral Researcher with Zhejiang University. His research interests include the analytical modeling of PMSM and iron loss analysis.



Xiaoyan Huang (Member, IEEE) received the B.E. degree in control measurement techniques and instrumentation from Zhejiang University, Hangzhou, China, in 2003, and the Ph.D. degree in electrical machines and drives from the University of Nottingham, Nottingham, U.K., in 2008.

From 2008 to 2009, she was a Research Fellow with the University of Nottingham. She is currently a Professor with the College of Electrical Engineering, Zhejiang University, where she is also working on electrical machines and drives. Her research interests

include PM machines and drives for aerospace and traction applications and generator systems for urban networks.



Ang Liu received the B.S. degree in electrical engineering from Zhejiang University, Hangzhou, China, in 2020, where he is currently pursuing the Ph.D. degree in electrical machines and drives.

His current research interests include the design and optimization of permanent-magnet machines for robotics and drones.



Zixuan Liu was born in Zhejiang, China, in 1998. He received the B.Eng. degree in electrical engineering from Zhejiang University, Hangzhou, China, in 2021, where he is currently pursuing the Ph.D. degree in electrical engineering.

His research interests include electrical machines and their control systems, and PM machine drives.



Lijian Wu (Senior Member, IEEE) received the B.Eng. and M.Sc. degrees in electrical engineering from the Hefei University of Technology, Hefei, China, in 2001 and 2004, respectively, and the Ph.D. degree in electrical engineering from The University of Sheffield, Sheffield, U.K., in 2011.

From 2004 to 2007, he was an Engineer with Delta Electronics (Shanghai) Company Ltd., Shanghai, China. From 2012 to 2013, he was with the Sheffield Siemens Wind Power Research Center, Shanghai, as a Design Engineer focusing on wind power generators. From 2013 to 2016, he was an Advanced Engineer with Siemens Wind Power A/S in Denmark. Since 2016, he has been with Zhejiang University, Hangzhou, China, where he is currently a Professor of electrical machines and control systems. His current research interests include the design and control of permanent magnet machines.



Tingna Shi (Member, IEEE) was born in Yuyao, China, in 1969. She received the B.S. and M.S. degrees in electrical engineering from Zhejiang University, Hangzhou, China, in 1991 and 1996, respectively, and the Ph.D. degree in electrical engineering from Tianjin University, Tianjin, China, in 2009.

She is currently a Professor with the College of Electrical Engineering, Zhejiang University. Her current research interests include electrical machines and their control systems, power electronics, and electric drives.